INSTITUTE OF PHYSICS PUBLISHING PLASMA PHYSICS AND CONTROLLED FUSION

Plasma Phys. Control. Fusion **46** (2004) 551–572 PII: S0741-3335(04)70218-3

# ELM characteristics in MAST

**A Kirk[1], G F Counsell[1], H R Wilson[1], J-W Ahn[1], R Akers[1], E R Arends[2], J Dowling[1], R Martin[1], H Meyer[1], M Hole[3], M Price[1], P B Snyder[4], D Taylor[1], M J Walsh[5], Y Yang[6] and the MAST team[1]**

[1] EURATOM/UKAEA Fusion Association, Culham Science Centre, Abingdon, Oxon OX14 3DB, UK
[2] FOM Institute for Plasma Physics 'Rijnhuizen', PO Box 1207, 3430 BE Nieuwegein, The Netherlands
[3] Applied and Plasma Physics, School of Physics, University of Sydney, NSW 2006, Australia
[4] General Atomics, PO Box 85608, San Diego, CA 92186-5608, USA
[5] Walsh Scientific Ltd, Culham Science Centre, Abingdon, Oxon OX14 3DB, UK
[6] Institute of Plasma Physics, Hefei 230031, People's Republic of China

Received 10 October 2003
Published 23 February 2004
Online at stacks.iop.org/PPCF/46/551 (DOI: 10.1088/0741-3335/46/3/009)

**Abstract**

Edge localized mode (ELM) characteristics in a large spherical tokamak (ST) with significant auxiliary heating are explored. High confinement is achieved in mega ampere spherical tokamak (MAST) at low ELM frequencies even though the ELMs exhibit many type III characteristics. These ELMs are associated with a reduction in the pedestal density but no significant change in the pedestal temperature or temperature profile, indicating that energy is convected from the pedestal region into the scrape-off layer. Power to the targets during an ELM arrives predominantly at the low field outboard side. ELM effluxes are observed up to 20 cm from the plasma edge at the outboard mid-plane and are associated with the radial motion of a feature at an average velocity of 0.75 km $s^{-1}$. The target balance observed in MAST is potentially rather favourable for the ST since H-mode access is facilitated in a regime where ELM losses flow mostly to the large wetted area, outboard targets and, in addition, the target heat loads are reduced by an even distribution of power between the upper and lower targets.

## 1. Introduction

An edge localized mode (ELM) is a violent repetitive fluctuation that appears near the edge of a plasma in some improved confinement (H-mode) regimes in magnetically confined plasmas. ELMs give rise to rapid transient increases in particle and energy fluxes to the divertor targets. Divertor power handling in a spherical tokamak (ST) may be of even greater significance than in conventional devices due to the reduced wetted area of the inboard strike-points due to the small major radius. A good understanding of the effects of ELMs on target power loading is

  

central to evaluating the potential of the ST as a future burning plasma device and can be used to refine estimations for ITER.

Plasmas in the mega ampere spherical tokamak (MAST) typically have a major radius, $R \sim 0.85\,\mathrm{m}$ and a minor radius $a \sim 0.65\,\mathrm{m}$. MAST has operated with plasma current up to $I_\mathrm{p} \sim 1.35\,\mathrm{MA}$ and is equipped with two neutral beam lines, which have so far provided deuterium injection into plasmas with total powers in excess of $P_\mathrm{NBI} \sim 2.9\,\mathrm{MW}$ (and will be capable of up to 5 MW). All the discharges described in this paper are for deuterium injection into deuterium plasmas. The toroidal field on axis is usually in the range $0.35\,\mathrm{T} < B_\phi < 0.55\,\mathrm{T}$, and due to the low aspect ratio, the toroidal field varies between 1.7 T at the inboard mid-plane and 0.25 T at the outboard. This strong variation across the plasma is a distinct feature of the ST.

MAST is well equipped with diagnostics for the study of ELMs, including a 300-point Thomson scattering system [1, 2], a fast reciprocating probe system equipped with a radial array of triple probes [3] and arrays of high spatial and temporal resolution Langmuir probes covering all four targets (3 mm spacing inboard, 10 mm spacing outboard) [4]. Figure 1 shows a poloidal cross section of the MAST vessel with a typical equilibrium superimposed. The locations of the main diagnostics used in this paper are indicated.

Preliminary results on ELMs were presented in [5] based on analysis of individual shots. This paper expands on these preliminary results and presents a systematic study of ELM

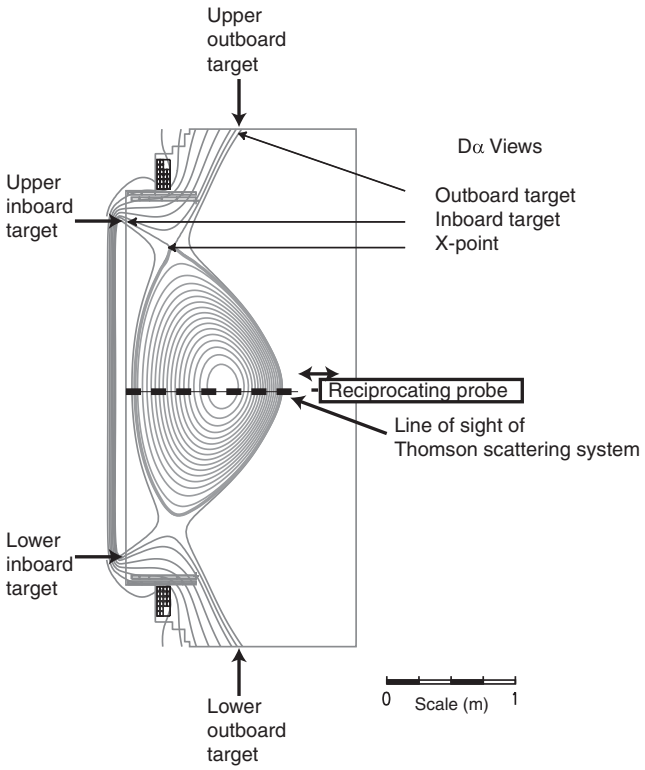


**Figure 1.** Poloidal cross section of MAST with a typical equilibrium. Shown on the figure are the locations of the targets, the mid-plane location of the reciprocating probes and the line of sight views of the Thomson scattering system and D$\alpha$ views of the X-point and upper inboard and outboard targets.

characteristics as follows: section 2 describes the global characteristics of the ELMs observed in MAST, including a discussion of their type. Section 3 describes the effect of ELMs on the target and section 4 describes evidence for the radial extent of ELMs.

## 2. ELM characterization

Figure 2 shows the D$\alpha$ emissions from the inboard and outboard targets as a function of time for six discharges with the same shaping, plasma current and density for different values of auxiliary heating power ($P_{\mathrm{NBI}}$). With increasing $P_{\mathrm{NBI}}$, the D$\alpha$ emissions increase at each ELM and the ELM frequency decreases. Figures 3(*a*) and (*b*) show the ELM frequency as a function of line-averaged density and $P_{\mathrm{SOL}}$ (defined as the sum of the Ohmic and auxiliary power input to the core plasma less the rate of change of stored energy and radiated power),

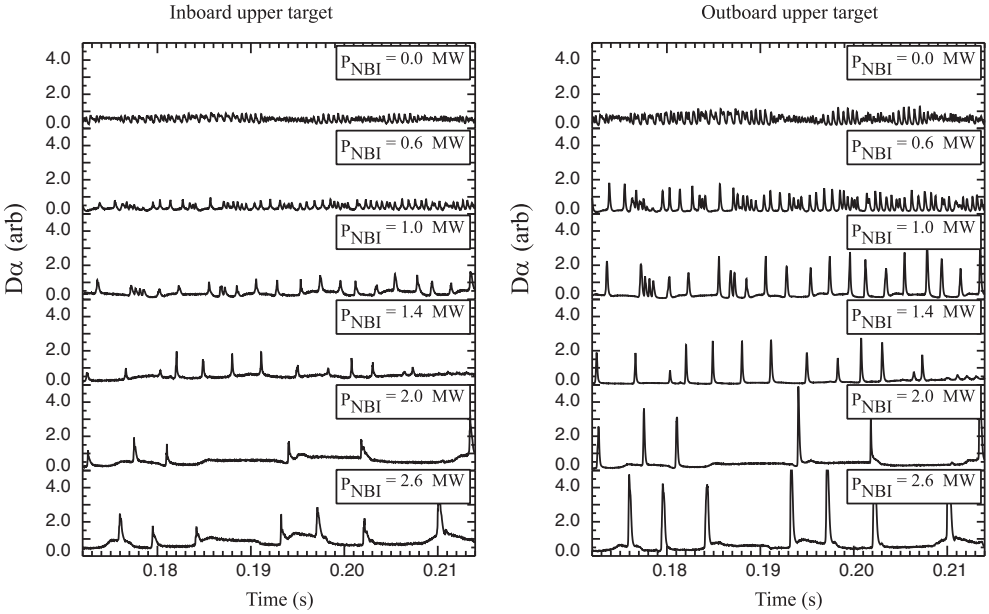


**Figure 2.** The D$\alpha$ signal at the upper inboard and outboard targets showing the variation of ELM frequency with auxiliary heating power at fixed plasma current and density.

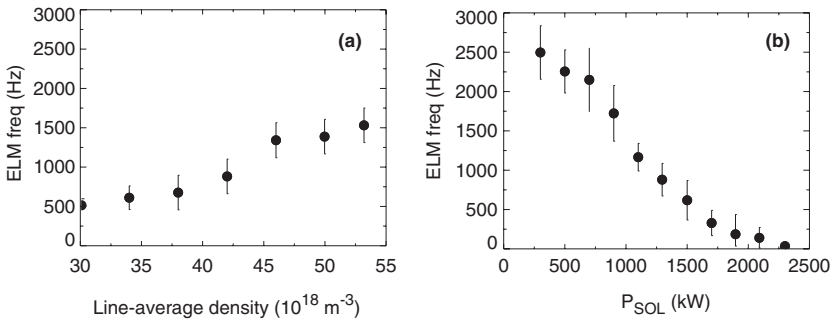


**Figure 3.** ELM frequency versus line-average density for $P_{\mathrm{SOL}}$ in the range 1.0–1.5 MW and ELM frequency versus $P_{\mathrm{SOL}}$ for line-average density in the range (30–40) $\times$ $10^{18}$ m$^{-3}$.

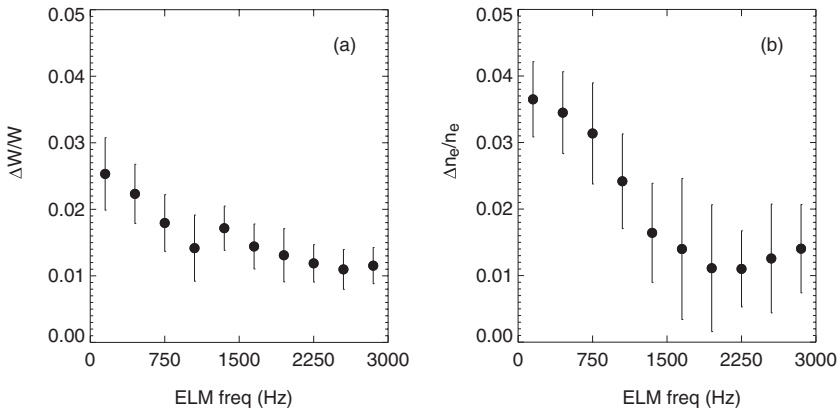


**Figure 4.** (*a*) The fraction of stored plasma energy released by an ELM (calculated using the change in stored energy from EFIT). (*b*) The fractional change in the line-average density due to an ELM.

respectively, using data from the entire database of analysed ELMy H-mode discharges. Each point represents the weighted mean of the data in that interval, and the error bar represents the standard deviation of the distribution. The decrease in ELM frequency with decreasing density and increasing power is typical of type III ELMs in conventional aspect ratio devices [6–8]. The energy released during the ELM has been calculated from the change in total stored energy ($\Delta W$) from EFIT equilibrium reconstruction [9], using EFIT runs with a 200 $\mu$s time step. The fraction of stored energy ($\Delta W/W$) released from the plasma due to an ELM is shown in figure 4(*a*). At low ELM frequencies, up to 3% of the stored energy is released by an ELM. A drop in the line-averaged density is observed at each ELM, and if the change of the global density profile is small, this drop can be used to estimate the fraction of particles released during an ELM. Figure 4(*b*) shows a plot of the fractional change in line-averaged density as a function of ELM frequency. At low ELM frequencies, up to 4% of the particles in the core are released during an ELM. These results are similar to those observed in COMPASS-D [10]. The fraction of stored energy released by an ELM is given by $\Delta W/W = \Delta n/n + \Delta T/T$, where the first term describes the convective losses and the second term the conductive losses. Bearing in mind the relative uncertainties in the methods used to calculate the respective quantities, the fact that $\Delta n/n$ is greater than or equal to $\Delta W/W$ at low ELM frequencies suggests that ELM conductive losses in MAST are small for beam powers up to 2.5 MW.

Figure 5(*a*) shows the variation of normalized confinement time, $H_{\rm H}(\equiv\tau_E/\tau_E^{\rm IPB98(y,2)}$, where $\tau_E$ is the energy confinement time and $\tau_E^{\rm IPB98(y,2)}$ is the ITER energy confinement time scaling [11]) with ELM frequency ($f_{\rm ELM}$) for a variety of MAST ELMy H-mode discharges. $H_{\rm H}$ rises rapidly from L-mode confinement levels ($H_{\rm H} \sim 0.5$) at $f_{\rm ELM} \gtrsim 1$ kHz to $H_{\rm H} \sim 1.5$ at $f_{\rm ELM} \lesssim 50$ Hz. High confinement is thus achieved in MAST at a low ELM frequency even though no clear transition to type I ELMs has been observed, e.g. an increase in ELM frequency with increased beam power. Figure 5(*b*) shows a plot of $H_{\rm H}$ versus the number of ELMs per energy confinement time, which follows a Fishpool-like scaling [12]. The distribution has been fitted to the Fishpool parametrization:

$$H = H_{\rm max} - af\tau_E(1 - {\rm e}^{-b/f\tau_E}),$$

where $f$ is the ELM frequency, $\tau_E$ is the energy confinement time and $H_{\rm max}$, $a$ and $b$ are parameters to be determined for the fit. The fitted curve shown in figure 5(*b*) gives a good

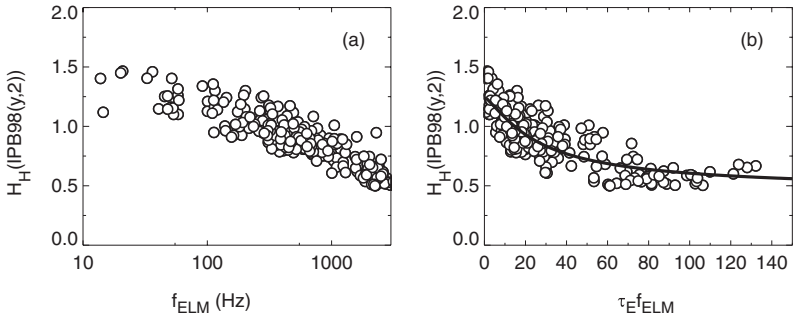


**Figure 5.** Variation of $\tau_E$ (normalized to IPB98($y$,2) scaling) with (*a*) ELM frequency and (*b*) the product of ELM frequency and confinement time. The line in (*b*) shows the results of a fit to Fishpool scaling.

description of the data and yields $H_{\max} = 1.25 \pm 0.1$, $a = 0.018 \pm 0.02$ and $b = 44 \pm 3$. The parameter $1/b \approx \Delta W/W \approx 2.2\%$ is consistent with the measured values given above.

One alternative way in which ELMs can be characterized is to consider the discharges in a plot of pedestal density versus pedestal temperature [13], where different regions can be associated with different ELM types. For example, type I ELMs appear to be associated with a line of approximately constant pedestal pressure [13], often in the vicinity of the ballooning stability boundary. It is therefore interesting to see how MAST fits this picture. Thus, the electron temperature, $T_{\rm p}$, and density, $n_{\rm p}$, at the top of the pedestal for a range of ELMy H-mode regimes have been determined from Thomson scattering profiles obtained during inter-ELM periods at a location 2 cm inboard of the radius of peak D$\alpha$ emission from the outboard mid-plane, $a_{\rm D\alpha}$. The radius $a_{\rm D\alpha} = 2$ cm is found empirically to provide a robust estimate for the location of the top of the density pedestal in MAST H-mode regimes. This constant offset is due to the fact that for pedestal densities greater than $3 \times 10^{19}\,{\rm m}^{-3}$ there is only a small change in density pedestal width with changing plasma conditions [14]. Figure 6 shows the outboard density and temperature profiles for shot 6252, which have been fitted using a modified hyperbolic tangent [15]. For the density profile, the location of the pedestal determined from this fit is in agreement, within the errors, with the radius $a_{\rm D\alpha} = 2$ cm. With the current Thomson scattering system, electron temperatures below 30 eV at the outboard side are subject to a large systematic error. In order to produce a modified hyperbolic tangent fit to the temperature profile, temperature values measured at the inboard side have been mapped to the outboard side (open circles in figure 6). The value of the pedestal temperature from the fit is in rough agreement with the value at the radius $a_{\rm D\alpha} = 2$ cm. In order to obtain the pedestal temperature at the outboard side for the bulk of discharges, the value at the location of the density pedestal has been used. Note that unless otherwise stated all calculations presented in this paper assume that $T_{\rm i}$ is equal to $T_{\rm e}$.

ELMy H-modes have been observed with $n_{\rm p}$ between $1.5 \times 10^{19}$ and $5.5 \times 10^{19}\,{\rm m}^{-3}$ and with $T_{\rm p}$ between around 80 and 200 eV. Figure 7 shows a plot of $T_{\rm p}$ against $n_{\rm p}$ where both are normalized to $B_\phi/q_{95}$, where $B_\phi$ is the toroidal field on axis and $q_{95}$ is the safety factor at the 95% flux surface. Often the density pedestal is expressed as a function of the Greenwald density ($n_{\rm GW}$). The MAST discharges shown in figure 7 have values of $n_{\rm p}/n_{\rm GW}$ in the range 0.15–0.90. In fact the normalized quantity $n_{\rm p}q_{95}/B_\phi$ can also be expressed in terms of the Greenwald density as $n_{\rm p}(q_{95}/B_\phi) = (f(S)/R)(n_{\rm p}/n_{\rm GW})$, where $R$ is the major radius and $f(S)$ is a function of the shaping of the plasma. On MAST, $f(S)/R$ has been found to be $\sim$8.8 for all the discharges in figure 7 and hence the Greenwald density limit occurs for $n_{\rm p}q_{95}/B_\phi \sim 8.8$.

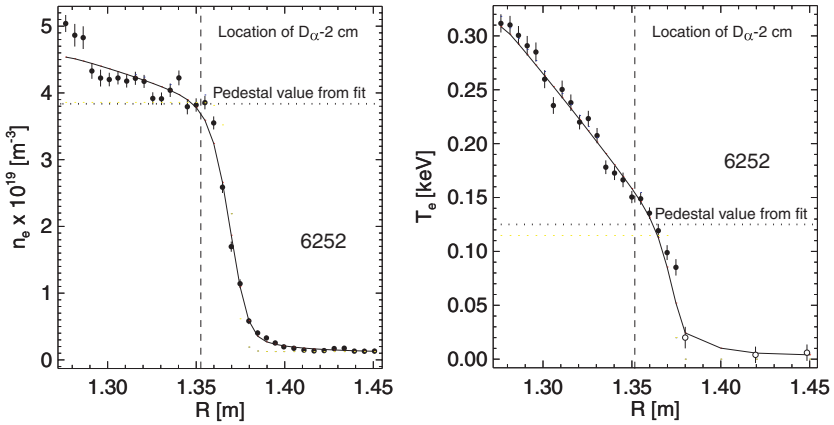


**Figure 6.** Thomson scattering profiles of the outboard edge density and temperature for shot 6252 with fit using a modified tanh function (——). The dotted horizontal line shows the pedestal height resulting from the fit, and the dashed vertical line shows the position of the pedestal as determined using the radius of the peak D$\alpha$ emission minus 2 cm. The open circles in the temperature profile are inboard values mapped to the outboard side (see text).

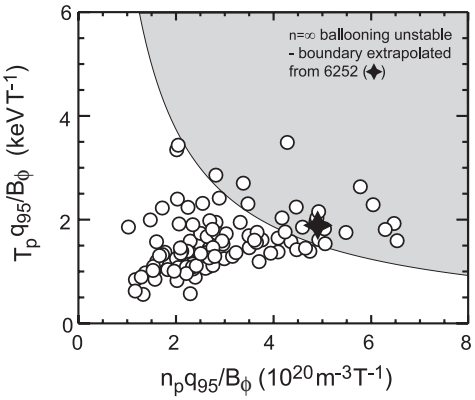


**Figure 7.** Edge $T$–$n$ space (normalized to $B_\phi/q_{95}$) showing the existence of ELMy H-modes from analysis of over 2500 shots. The region of instability to $n = \infty$ ideal ballooning is shaded.

The advantage of the $q_{95}/B_\phi$ normalization is that it makes machine to machine comparison more straightforward, and the ballooning stability can be approximately represented by a curve $(n_p q_{95}/B_\phi) * (T_p q_{95}/B_\phi) =$ constant, neglecting the effect of any variations in the magnetic shear and pedestal width. To determine the constant, a carefully reconstructed equilibrium for discharge 6252 has been used that is chosen because it is close to marginal stability to $n = \infty$ ballooning modes, as predicted by the IDBALL code [16]. The pressure in this discharge is then scaled until marginal stability is found, and then the constant can be determined. The shaded area in figure 7 represents the region of instability to $n = \infty$ ballooning modes expected from this analysis. One striking feature is that a significant number of discharges lie close to the stability boundary. An estimate can also be made of the peeling mode stability for 6252. This requires an estimate of the edge current density, which is assumed to be dominated by the bootstrap current. This is calculated from the measured pressure profile, and according to the analytic stability criterion [17], 6252 is expected to be unstable to the peeling mode. Discharge 6252 is typical of many of the ELMy discharges lying in the vicinity of the $n = \infty$

ballooning stability boundary and thus would be expected to be unstable to coupled peeling–ballooning modes. These modes are thought to be associated with large type I ELMs, and yet as discussed above, the ELMs show characteristics more like type III.

In order to resolve this apparent contradiction, we have performed a more detailed study of the pedestal stability using the ELITE code [18]. This code evaluates the stability to finite $n$ ideal MHD modes, which are localized in the plasma edge region. Toroidal mode numbers in the range $6 < n < 50$ were scanned, and over the whole of this range no ballooning-type modes were found. Instead, only highly localized peeling modes could be found at certain toroidal mode numbers (e.g. $n = 8$ is unstable). This can be understood in terms of the linear theory of ballooning modes [19], which predicts that the finite $n$ corrections are stabilizing and, because of the rather narrow pedestal widths in MAST [20], these corrections are enhanced and could be suppressing the ballooning-type modes. Thus, the absence of a strong linear ballooning mode drive for realistic $n$ (the higher $n$ are likely to be stabilized by diamagnetic effects) in the narrow pedestal of MAST may provide a possible explanation for why MAST does not show clear characteristics for type I ELMs despite the pedestal pressure gradients being in the vicinity of the $n = \infty$ ballooning stability boundary.

## 3. Effect of ELMs at the target

The upper limit on the tolerable size of an ELM is dictated by surface ablation at the targets. The target heat load is determined by the temporal duration of the heat pulse and the target wetted area, which depends on the SOL width and the strike-point radius. In a ST the wetted area at the inboard target is considerably smaller than for a similarly sized conventional aspect ratio device, and hence an understanding of the distribution of energy released by an ELM between the outboard and inboard targets is even more essential.

### *3.1. Outboard/inboard target loads and the effect of magnetic configuration*

The most common operating mode for MAST is the disconnected double-null (DDN), in which the two X-points lie on different flux surfaces with the gap between these at the outboard mid-plane, $\delta r_{\mathrm{sep}}$ being of the order of the ion gyro-radius. Figure 8 shows a plot of the difference in power at the upper and lower targets expressed as a fraction of the total power as a function of $\delta r_{\mathrm{sep}}$ for a controlled series of shots with a constant $P_{\mathrm{SOL}}$. The power density arriving at each of the target probes was calculated from the ion saturation current density ($J_{\mathrm{SAT}}$) and the electron temperature ($T_{\mathrm{e}}$) using $P = \gamma J_{\mathrm{SAT}} T_{\mathrm{e}}$, where $\gamma$ is the sheath transmission coefficient. A value of $\gamma = 7$ has been used, which assumes that $T_{\mathrm{i}} = T_{\mathrm{e}}$ [21].

For this series of Ohmic discharges, H-mode access is achieved for small $\delta r_{\mathrm{sep}}$, i.e. when the plasma is close to a connected double-null (CDN) configuration. Up–down power balance is achieved for $\delta r_{\mathrm{sep}} \sim 2$ mm with the active X-point in the upward direction required to balance the ion $\nabla B$ drift direction, which is towards the lower targets. On average the up–down power balance is maintained both at the ELM peaks and during the inter-ELM periods.

Figure 9(*a*) shows a plot of the ratio of power arriving at the outboard strike-points (sum of upper and lower) to that at the inboard strike-points ($R_{\mathrm{oi}}$) as a function of $\delta r_{\mathrm{sep}}$ for the same series of shots. In the L-mode cases the ratio $R_{\mathrm{oi}}$ is dependent of $\delta r_{\mathrm{sep}}$, which determines the degree of isolation between the inboard and outboard scrape-off layers (SOLs). A similar effect was observed on DIII-D [22]. For the series of discharges in figure 9(*a*) H-mode is achieved at small $\delta r_{\mathrm{sep}}$. Therefore, in order to determine the ratio of $R_{\mathrm{oi}}$ for L-mode discharges close to CDN a similar set of discharges was performed using outboard gas puffing only, which is found to inhibit H-mode access. In these L-mode discharges close to CDN the mean ratio,

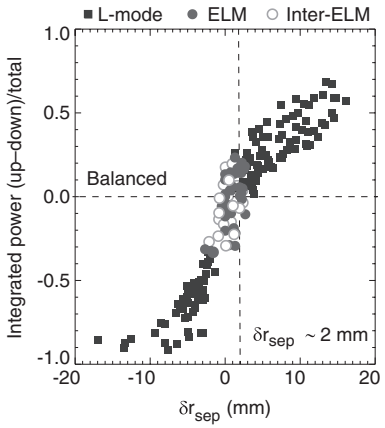


**Figure 8.** The fractional difference in power arriving at the upper and lower targets as a function of $\delta r_{\rm sep}$.

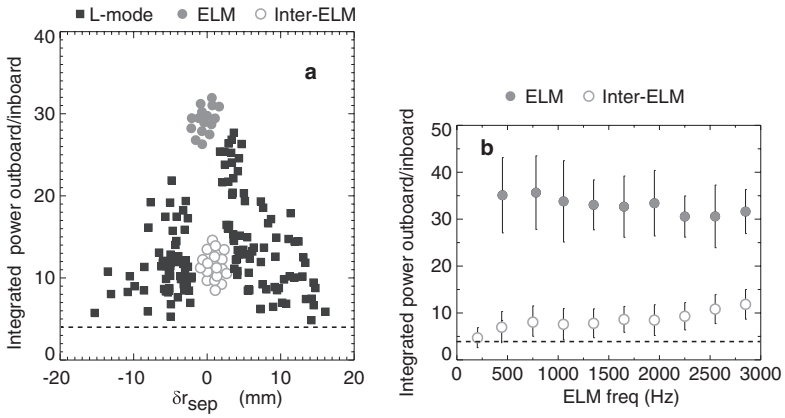


**Figure 9.** The ratio of the power to outboard over inboard targets: (*a*) versus $\delta r_{\rm sep}$ for L-mode and H-mode discharges at constant $P_{\rm SOL}$ and (*b*) versus ELM frequency for ELM and inter-ELM periods during H-mode discharges with $|\delta r_{\rm sep}| < 2$ mm. The dashed line shows the ratio of outboard to inboard separatrix areas. The ELMy H-mode data in (*a*) have a mean ELM frequency of 2800 Hz and are a subset in the highest frequency data point of (*b*).

$R_{\rm oi}$, is 30 (with a spread between 25 and 40), and since $P_{\rm outer} + P_{\rm inner} \approx P_{\rm SOL}$, this implies that 97% of the power leaving the core flows into the outboard SOL. This is much larger than would be expected from the ratio of the surface area of the separatrices (≈4) and would suggest that the outboard power efflux is augmented by other processes, perhaps turbulence related to the bad curvature and very low field on the outboard mid-plane.

For the H-mode case, a data 'box-car' technique [4] has been used to obtain target profiles both at ELM peaks and inter-ELM, during regular ELMing periods. In this method the target profiles are built up at each strike-point by requiring that the probe information be collected within 30 $\mu$s of either the ELM peak or the inter-ELM time (defined as being halfway between adjacent ELMs). The $R_{\rm oi}$ ratio at the ELMs is similar to the L-mode ratio for the same $\delta r_{\rm sep}$; however, the inter-ELM ratio is much smaller.

Figure 9(*b*) shows a histogram of how the ratio $R_{\rm oi}$ changes as a function of ELM frequency, using data from more than 100 analysed ELMy H-mode discharges when the plasma is near to

CDN with similar elongation (≈1.9), triangularity (≈0.4) and $q_{95}$(≈5) for a range of auxiliary heating powers (0–2.5 MW). Each point represents the weighted mean of the data in that bin, and the error bar represents the standard deviation of the distribution. The ELMy H-mode data in figure 9(*a*) have a mean ELM frequency of 2800 Hz and are a subset in the highest frequency data point of figure 9(*b*). Independent of ELM frequency, most of the power in the ELMs flows to the outboard strike-point, with more than 95% of the power reaching the outboard side. In the inter-ELM period the ratio $R_{\mathrm{oi}}$ tends to the ratio of the outboard to inboard separatrix surface area (≈4) at a low ELM frequency. Thus, the additional processes, which increased the relative power flow to the outboard side in L-mode and at the ELMs, are absent or strongly suppressed. For comparison, in JET the ratio $R_{\mathrm{oi}}$ at an ELM is approximately 1.0 [23], while ASDEX-U has a ratio of 0.5 [24].

The reduction of $R_{\mathrm{oi}}$ in inter-ELM periods as the ELM frequency reduces may be due to the time taken for the transport in the SOL to recover following an ELM. Most of the ELM power goes to the outboard side, and it is only at low ELM frequencies that there is enough time between ELMs for complete recovery of the SOL transport. Only when this is achieved would an $R_{\mathrm{oi}}$ value as low as might be expected from the ratio of surface areas be attained.

The target balance observed in MAST is potentially rather favourable for the ST since H-mode access is facilitated in a regime where ELM losses flow mostly to the large wetted area, outboard targets, and in addition, the target heat loads are reduced by an even distribution of power between the upper and lower targets.

### *3.2. ELM versus inter-ELM target characteristics*

Figure 10 shows a plot of the ratio of the power arriving to the targets at the ELM peak to that inter-ELM as a function of ELM frequency for the outboard and inboard strike-points. First, independent of frequency the ratio is ≈1 for the inboard strike-points, which is consistent with very little of the power released by the ELMs reaching the inboard targets. It should be remembered that the error bars on the figure represent the standard deviation of the data points in that bin. The individual data points for the inboard strike-point are compatible with unity within their associated measurement error. For the outboard targets, the ratio rises with decreasing ELM frequency, reaching an average ratio of greater than 5 for ELM frequencies below 250 Hz.

Figure 11 shows the ratio at the ELM peak to the inter-ELM period for $J_{\mathrm{SAT}}$ and $T_{\mathrm{e}}$ at the strike-point. The data come from both the upper and lower strike-points, and since there is no difference in the two distributions, both samples have been combined in the figure. The $J_{\mathrm{SAT}}$

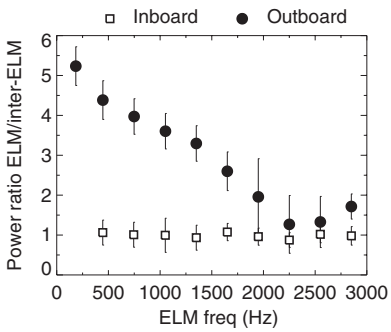


**Figure 10.** Ratio of the power at the ELM to the inter-ELM for the inboard and outboard strike-points as a function of ELM frequency.

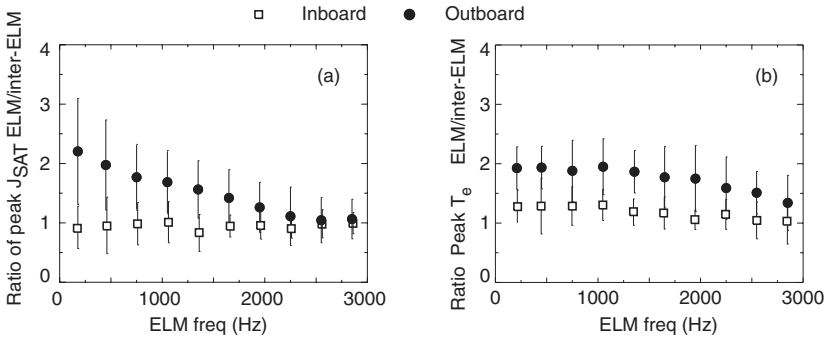


**Figure 11.** (*a*) The ratio of peak $J_{SAT}$ value and (*b*) the ratio of the value of $T_e$ at the ELM peak to the inter-ELM period versus ELM frequency for the inboard and outboard strike-points.

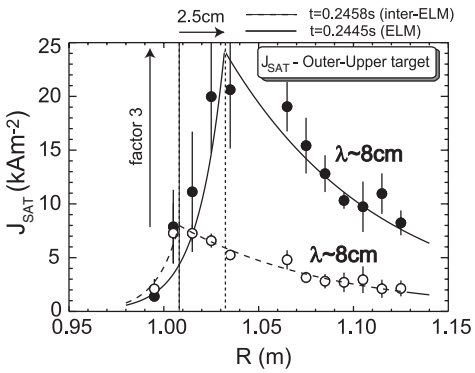


**Figure 12.** The $J_{SAT}$ profiles from the target Langmuir probes at the outboard upper target at the ELM peak and in the inter-ELM period.

at the outboard side rises from a factor of 1.2 at high ELM frequencies to a factor of 2.2 at low ELM frequencies. The electron temperature at the outboard side rises to a factor of 1.8 at the ELM relative to inter-ELM for ELM frequencies less than 1000 Hz. The ratio of power shown in figure 10 includes the changes in target area (from the strike-point position and heat flux width discussed later) in addition to the changes in $J_{SAT}$ and $T_e$ shown in figure 11.

Figure 12 shows the $J_{SAT}$ probe profiles at the outer upper target at an ELM and in the following inter-ELM period. As can be seen, although the $J_{SAT}$ increases, there is effectively no change in the width of the profile; however, the position of the peak of the distribution moves by 2.5 cm. Figure 13 shows a plot of the difference between the position of the peak and the width of the $J_{SAT}$ profile at the ELM peak relative to the inter-ELM period versus ELM frequency for the inboard and outboard strike-points. The arrival of the ELM at the outboard target is accompanied by an outward shift in radius of the peak position by up to 3 cm for low frequency ELMs. The H-mode strike-point widths are 20% narrower than the L-mode widths; however, there is no significant change in the width of the distribution from inter-ELM to ELM.

Emission of D$\alpha$ light in the divertor region has been used to determine the duration of the ELM peak ($\approx$300 $\mu$s) and the inter-ELM period. During these two periods the probe power has been integrated over time to produce the energy arriving at the probes. Figure 14 shows a plot of the energy deposited on the targets as a function of ELM frequency. The energy deposited at the inboard targets is greater during the inter-ELM period than at the ELM. This is because

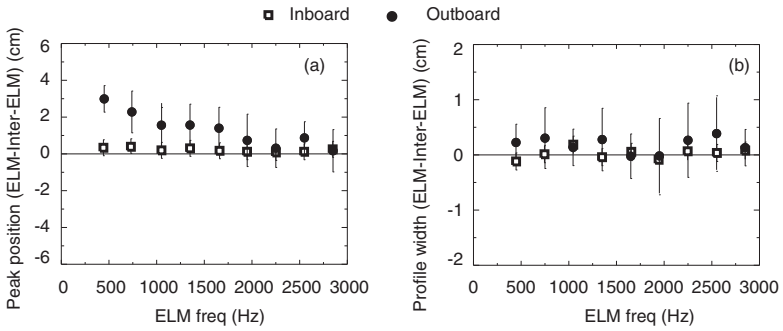


**Figure 13.** Difference in the position of the peak and width of the $J_{SAT}$ profile at the ELM peak relative to the inter-ELM period versus ELM frequency for the inboard and outboard strike-points.

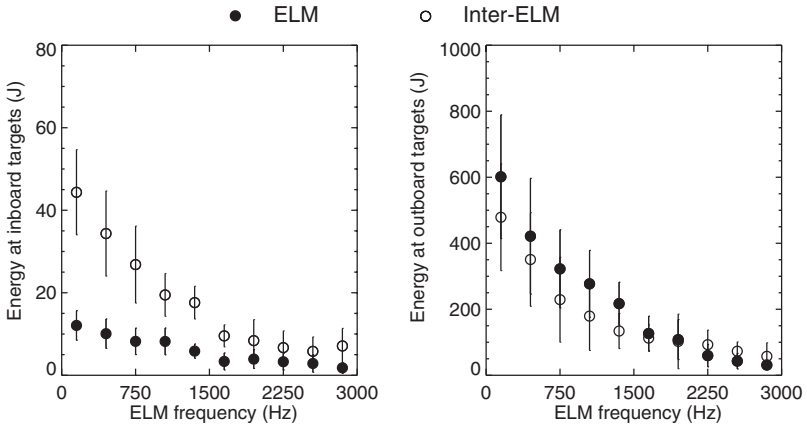


**Figure 14.** Energy measured at the ELM and in the inter-ELM period as a function of ELM frequency using the target Langmuir probes at the inboard and outboard targets.

very little power from the ELM reaches the inboard side and the inter-ELM period is large compared with the duration of the ELM and therefore becomes more noticeable as the ELM frequency decreases. For the outboard targets the ratio of energy deposited during an ELM to that during the inter-ELM period is $\approx$1, independent of frequency. The energy deposited increases with decreasing ELM frequency. Note, as in all power calculations presented in this paper, $T_i$ is assumed equal to $T_e$.

### *3.3. Overall power balance*

Figure 15(*a*) shows a plot of the total power arriving at the target probes versus the power into the SOL ($P_{SOL}$) for a range of L-mode discharges. $P_{SOL}$ is defined as the sum of the Ohmic and auxiliary power input to the core plasma less the rate of change of stored energy and radiated power. The mean radiated power loss, which includes the effects of charge exchange, is $\sim$15% (the $\sigma = 5\%$) and is determined from bolometry. Good power accounting is achieved for the whole range of shots, indicating that the method used to calculate the power to the probes, described in section 3.1, is valid for L-mode discharges. Figure 15(*b*) shows the plot for H-mode shots in inter-ELM periods. Only long inter-ELM periods (corresponding to ELM frequencies of less than 500 Hz) can be used since EFIT has to be run on several time slices

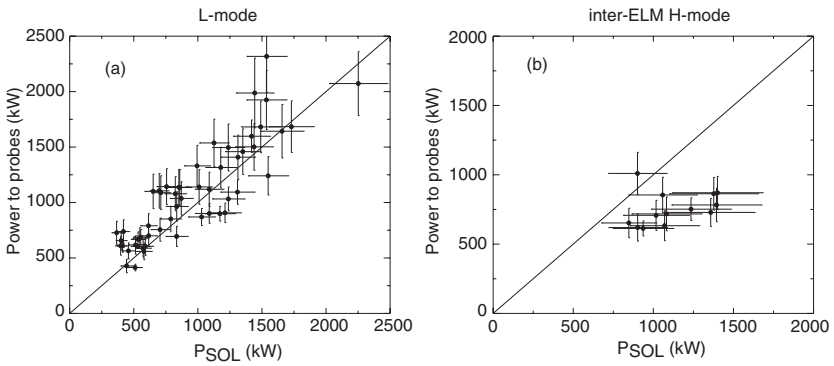


**Figure 15.** Total power arriving at the target probes versus the power into the SOL ($P_{\mathrm{SOL}}$) for (*a*) L-mode shots and (*b*) the inter-ELM period of H-mode shots.

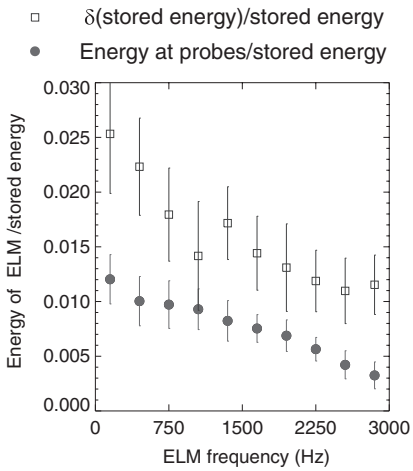


**Figure 16.** The fraction of stored plasma energy released by an ELM measured by the target probes and from the change in stored energy from EFIT.

in order to calculate $P_{\mathrm{SOL}}$. In inter-ELM periods there is a loss of power accounting. The ratio of $P_{\mathrm{SOL}}/P_{\mathrm{target}}$ is $1.4 \pm 0.3$. A possible way of resolving this loss of power accounting would be if the ion temperature exceeded the electron temperature by a factor of 2. This will be discussed later.

The energy released during the ELM has been calculated from the change in total stored energy ($\Delta W$) from EFIT [9], using EFIT runs with a 200 $\mu$s time step. The fraction of stored energy ($\Delta W/W$) released from the plasma at an ELM is shown in figure 16 together with that calculated from the energy arriving at the probes. $\Delta W$ is approximately a factor of 2 greater than the value obtained from the probes. Since the bolometry does not indicate a significant increase in radiated power and there is no evidence for interactions outside the divertor region (except with the reciprocating probe when less than $\approx$30 cm from the plasma edge), a possible explanation is that a large fraction of the ELM energy flows in the ion channel, i.e. $T_{\mathrm{i}}$ is substantially greater than $T_{\mathrm{e}}$. In JET, an IR camera has been used to determine the total deposited heat (ion plus electron), and it is found that global energy balance is achieved with error bars of 10–20% [25]. In order to give power accounting in MAST the sheath transmission coefficient, $\gamma$, would have to be increased from 7 to 14, corresponding to $T_{\mathrm{i}} \approx 4T_{\mathrm{e}}$. In fact in

discharge 6953, an ELMy H-mode shot for which $T_i$ measurements are available, the edge $T_i$ measured is already at least two times the edge $T_e$ during an inter-ELM period [26], and ion temperatures up to six times the electron temperature have been observed in the JET SOL [27]. In JET the fact that $T_i$ is larger than $T_e$ is due to fact that the ions are convected from further inside the pedestal than the electrons due to finite Larmor radius effects. Due to the low field on the outboard side of MAST, these effects could be even larger in MAST.

### *3.4. ELM rise times*

A critical parameter that determines the compatibility of ELMs with an acceptable divertor target lifetime is the duration of the ELM power load. The power deposition time in the divertor varies from 100–600 $\mu$s on JET and JT-60U to 200–300 $\mu$s on DIII-D and 300 $\mu$s or more on ASDEX-U [28]. When an ELM occurs, the pedestal plasma loses energy towards the divertor plate, through both the electron and ion channels, during a time $\tau_{ELM}$. The duration of the ELM process (a few 100 $\mu$s) is short compared with the equilibration time (10 ms), and hence the expelled ions and electrons have no time to equilibrate. Due to the larger thermal parallel conductivity, the electron temperature at the divertor target will increase in a few microseconds and a new sheath will be established. As a consequence, the energy will be delivered to the divertor in timescales typical of the ion parallel flow. It has been reported [29] that the ELM rise time as seen at the target by a fast IR camera scales as $\tau_{ELM} \approx 10^{-4}(\tau_{\|})^2$, where $\tau_{\|}$ is the ion parallel transit time from the pedestal to the target calculated using the pedestal ion temperature. In the following sections, data from MAST are compared with this scaling; however, due to the lack of a fast IR camera on MAST and routine pedestal $T_i$ measurements, alternative methods are required to calculate $\tau_{ELM}$ and $\tau_{\|}$. These methods are described in the following sections.

*3.4.1. Determination of $\tau_{ELM}$.* Figure 17 shows the $J_{SAT}$ and $T_e$ signals from the target Langmuir probes together with the target D$\alpha$ signal. The peak in the $T_e$ signal is earlier than the peak in either the D$\alpha$ signal or the $J_{SAT}$ signals, and the rise time of the $T_e$ signal is faster (see also figure 19). Both the $J_{SAT}$ and $T_e$ signals start to rise earlier than the D$\alpha$ signal. The rise in electron temperature before the rise in the $J_{SAT}$ has been observed previously in JET [30]. It can be explained as being due to the short time required for parallel conduction of the electron thermal energy compared with the convection time of the ions. It is interesting to note that the D$\alpha$ signal starts to rise on the timescale of the particle flux arrival.

The peak position of the D$\alpha$ signal has been used to define the time of the ELM. For each target probe characteristic recorded, the corresponding time relative to the nearest ELM has

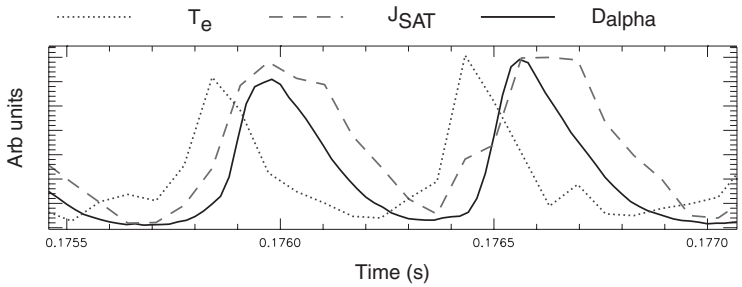


**Figure 17.** The target D$\alpha$ signal, $J_{SAT}$ and $T_e$ for shot 4253.

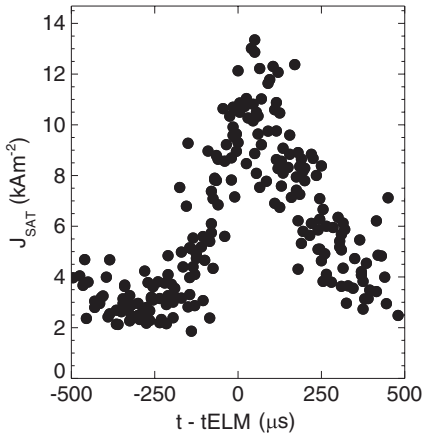


**Figure 18.** Peak $J_{SAT}$ versus difference in time to the peak of the D$\alpha$ distribution of the nearest ELM for shot 4251.

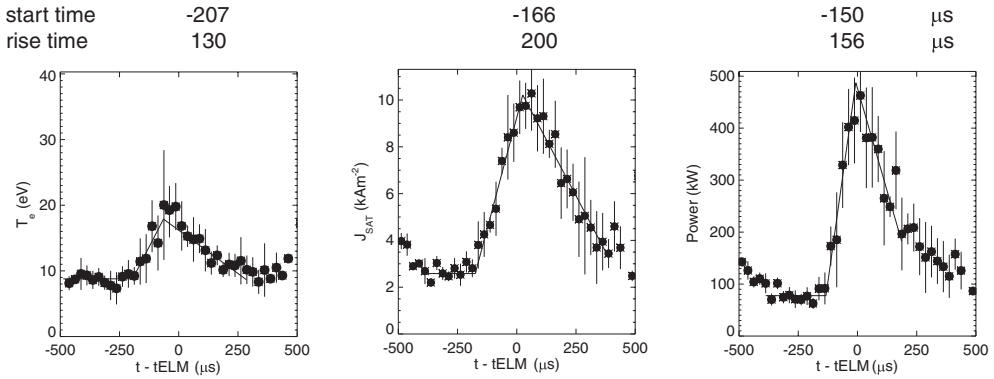


**Figure 19.** The $T_e$, $J_{SAT}$ and power distribution relative to the ELM peak for shot 4251.

been calculated for a period of regular ELMs in a discharge. Figure 18 shows a plot of the peak $J_{SAT}$ obtained as a function of this time difference for shot 4251.

The values of the peak in each radial $J_{SAT}$ profile (and similar data for the peak $T_e$ and power) have been histogrammed and the weighted mean of the data and standard deviation of the data calculated in each bin. As can be seen from figure 19, the $T_e$ distribution does start to rise earlier than the $J_{SAT}$, and the rise time of $T_e$ is faster than $J_{SAT}$. As a result the power calculated from the product of $T_e$ and $J_{SAT}$ is narrower than the $J_{SAT}$ distribution. However, as was seen in section 3.3, in order to get correct power accounting, $T_i$ must be greater than $T_e$ and hence significant power is expected to flow in the ion channel. Therefore the best estimation of the power rise time of the ELM is the $J_{SAT}$ rise time. The rise time determined by this method has been calculated for a set of shots (see table 1).

*3.4.2. Determination of* $\tau_\parallel$. $\tau_\parallel$ is the ion parallel transit time from the pedestal to the target, given by [29]

$$\tau_\parallel = \frac{2L_\parallel}{c_s}, \tag{1}$$

**Table 1.** The ELM rise time at the target probes and methods of calculating the parallel energy loss time.

| Shot number | Power rise time ($\mu$s) | $J_{SAT}$ rise time ($\mu$s) | $T_e$ rise time ($\mu$s) | $T_e$ from TS (eV) | X-point–target D$\alpha$ time difference ($\mu$s) | $\tau_\parallel$ $T_i = T_e$ ($\mu$s) | $\tau_\parallel$ from target D$\alpha$ time difference ($\mu$s) | Derived value of $T_i/T_e$ |
|---|---|---|---|---|---|---|---|---|
| 4251 | 156 | 200 | 130 | 130 | 35 | 283 | 128 | 4.4 |
| 4253 | 164 | 231 | 141 | 130 | 35 | 339 | 125 | 5.6 |
| 4438 | 141 | 185 | 131 | 93 | 24 | 317 | 91 | 6.2 |
| 4441 | 163 | 227 | 170 | 160 | 39 | 184 | 150 | 2.6 |
| 5748 | 159 | 193 | 177 | 98 | 31 | 253 | 119 | 3.5 |
| 5749 | 150 | 187 | 149 | 102 | 27 | 257 | 97 | 5.5 |
| 6234 | 165 | 218 | 138 | 102 | 32 | 192 | 121 | 3.4 |

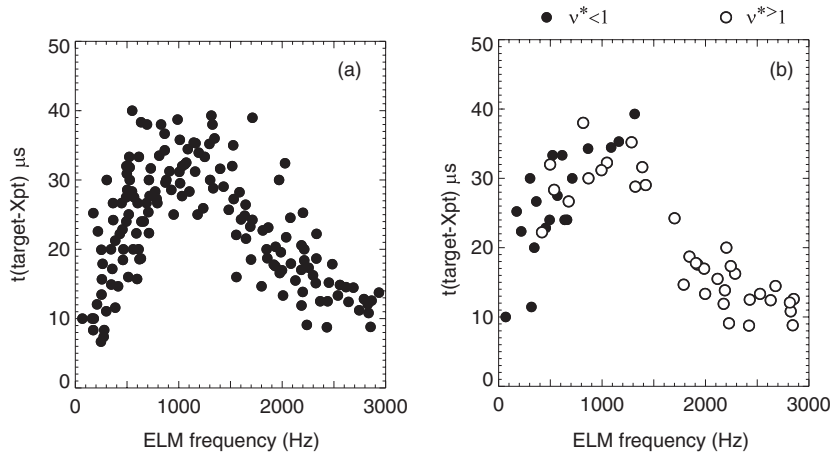


**Figure 20.** Time difference between the peak of the D$\alpha$ at the target and the X-point as a function of ELM frequency: (*a*) for all data and (*b*) for the data set close to the Thomson scattering time for which the collisionality ($\nu^*$) can be calculated.

where $2L_\parallel$ is the target to target connection length and $c_s$ is the ion sound speed for the pedestal ion temperature. In MAST only a measure of the pedestal electron temperature is regularly available. The values calculated for $\tau_\parallel$ assuming $T_i = T_e$ are given in table 1. However, we have already seen that assuming $T_i = T_e$ does not give energy balance during an ELM. Therefore, making this assumption may also underestimate $c_s$ and hence overestimate $\tau_\parallel$. Therefore a second method of determining $\tau_\parallel$ has been used based on the difference in time of the peak in D$\alpha$ emission at two points along the connection length, namely at the X-point and at the target. This may in any case be a more accurate method for determining $\tau_\parallel$.

The delay between the peak in D$\alpha$ emissions is assumed to be due to the time taken for the ions to travel from the X-point to the target, where they cause recycling and hence generate the source of neutrals for the enhanced D$\alpha$ emission. By comparing the distance from the X-point to the target with the total connection length, this delay can be used to determine $\tau_\parallel$. The difference in peak time between the X-point signal and the target signal has been studied as a function of ELM frequency and is shown in figure 20(*a*). As can be seen, the time difference changes with ELM frequency.

A value of $\tau_\parallel$ can only be determined from this method when the flow is convective and hence when both the electron and ion collisionalities are low enough. All the data presented

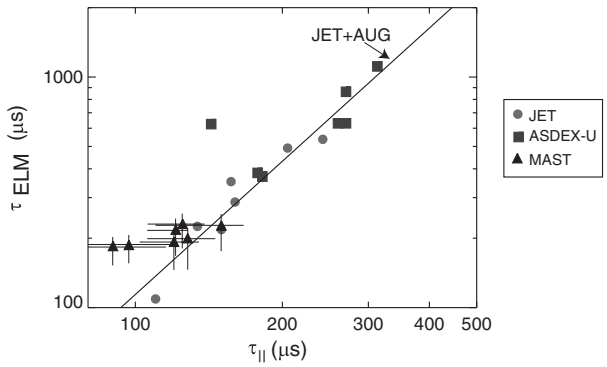


**Figure 21.** ELM rise time ($\tau_{\mathrm{ELM}}$) versus ion parallel transit time ($\tau_{\|}$) for data from JET, ASDEX-U and MAST.

in this paper are consistent with $T_{\mathrm{i}} \geqslant T_{\mathrm{e}}$; therefore, the electron collisionality will always be bigger than the ion collisionality and hence a cut on electron collisionality ($\nu_{\mathrm{e}}^{*}$) is used. Figure 20(*b*) shows the data split up into low ($\nu_{\mathrm{e}}^{*} < 1$) and high collisionality ($\nu_{\mathrm{e}}^{*} > 1$), with the collisionality having been calculated using, where available, electron temperature and density values at the pedestal from the Thomson scattering system. The collisionality is lower for low frequency ELMs and it is only for ELM frequencies less than 1 kHz that the collisionality is low enough for the ion flow to be considered convective and hence for a sensible value of $\tau_{\|}$ to be extracted. Figure 20(*b*) shows that for discharges where the collisionality is less than 1 the time difference rises roughly linearly with ELM frequency. The ratio of the connection length between the X-point and the target to the total connection length is used to calculate a value of $\tau_{\|}$ and is given in table 1. These values of $\tau_{\|}$ have then been used to derive a value for the ratio $T_{\mathrm{i}}/T_{\mathrm{e}}$ using equation (1). These ratios are consistent with the estimate $T_{\mathrm{i}} \approx 4T_{\mathrm{e}}$ required to give global power accounting during an ELM (see section 3.3).

*3.4.3.* $\tau_{\mathrm{ELM}}$ *versus* $\tau_{\|}$. Figure 21 shows a plot of the ELM rise time ($\tau_{\mathrm{ELM}}$) (calculated using the target $J_{\mathrm{SAT}}$ values) versus $\tau_{\|}$ (using the measurement of the time delay in the peak of the D$\alpha$ emissions) compared with the values of $\tau_{\mathrm{ELM}}$ versus $\tau_{\|}$ from JET and ASDEX-U. A previous fit to the JET and ASDEX-U data showed that $\tau_{\mathrm{ELM}} \propto (\tau_{\|})^2$ [29]. Within the errors the MAST data fall in the area of the plot predicted by this scaling.

The rise time at the targets will clearly depend on the time taken for the particles and energy to reach the target, but it will also depend on the lifetime of the ELM, i.e. the time over which the ELM is releasing particles and energy into the SOL. The drawback of the scaling presented above is that it would predict that as $\tau_{\|} \to 0$, then $\tau_{\mathrm{ELM}} \to 0$; i.e. it does not allow for any MHD time of the ELM. A better fit to the data may be to use $\tau_{\mathrm{ELM}} = \tau_{\mathrm{MHD}} + \tau_{\|}$, where $\tau_{\mathrm{MHD}}$ is the time over which particles are leaving the core plasma due to the ELM, i.e. it is the 'real' lifetime of the ELM ignoring any SOL transport times. Performing such a fit to the MAST data gives $\tau_{\mathrm{MHD}} = 87 \pm 25\,\mu$s.

## 4. ELM characterization at the mid-plane

Figure 22 shows Thomson scattering profiles at the outboard mid-plane obtained at two times with respect to the time of peak D$\alpha$ emission at the divertor target, $t_{\mathrm{ELM}}$. Just before the ELM ($t_{\mathrm{ELM}} - 740\,\mu$s), the core density profile is very flat with a steep edge density gradient, $\mathrm{d}n_{\mathrm{e}}/\mathrm{d}r \sim 1.5 \times 10^{21}\,\mathrm{m}^{-4}$. In contrast, the core temperature profile is rather peaked with a

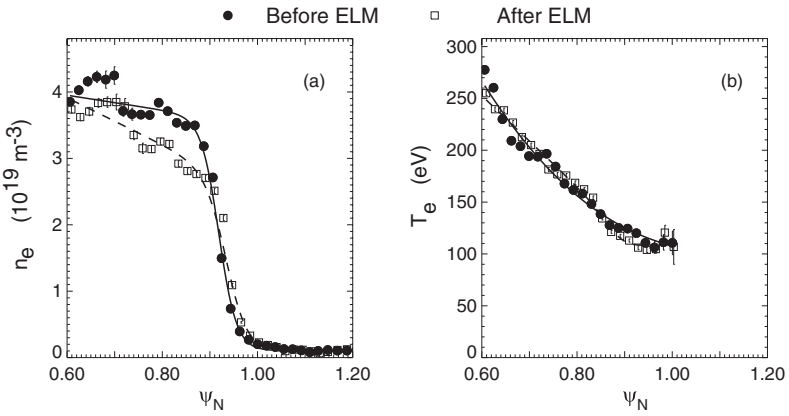


**Figure 22.** Thomson scattering profiles of the outboard edge density and temperature for two 'identical' 650 kA H-mode discharges, with 1.4 MW of neutral beam heating, at two times with respect to a similar ELM in each; before ($t_{\mathrm{ELM}} - 740\,\mu$s) and after ($t_{\mathrm{ELM}} + 540\,\mu$s) the peak in divertor D$\alpha$ emission.

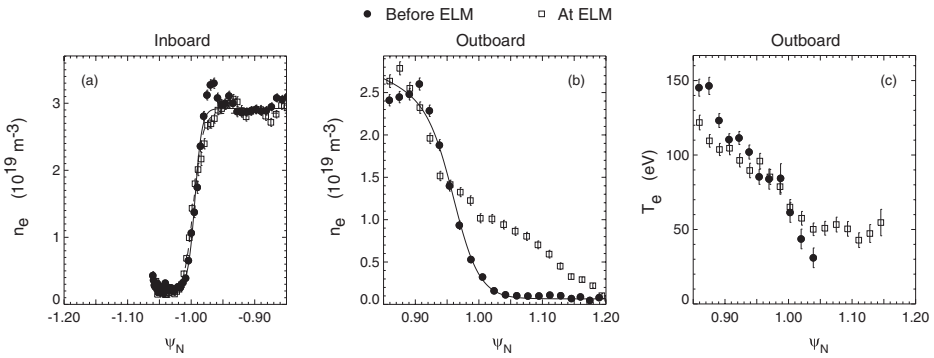


**Figure 23.** Thomson scattering profiles of the inboard and outboard edge density and temperature in normalized flux co-ordinates for two 'identical' 650 kA H-mode discharges, with 0.8 MW of neutral beam heating, at two times with respect to a similar ELM in each; before ($t_{\mathrm{ELM}} - 770\,\mu$s) and at ($t_{\mathrm{ELM}} - 5\,\mu$s) the peak in divertor D$\alpha$ emission. The existence of electron temperature data during the ELM from the Thomson scattering system for $\psi_{\mathrm{N}} > 1.05$ is a consequence of improved photon statistics arising from the enhanced electron density in this region during the ELM.

shallow edge gradient, $\mathrm{d}T_{\mathrm{e}}/\mathrm{d}r \sim 1500\,\mathrm{eV\,m^{-1}}$. Just after the ELM ($t_{\mathrm{ELM}} + 540\,\mu$s), there is little change in the edge temperature profile but there is a reduction in $n_{\mathrm{p}}$. This is consistent with $\Delta W$ being dominated by convective losses from the pedestal region, with little of the energy being conducted into the SOL, at least for the ELMs explored in figure 22. The convective loss calculated for this ELM from the change in density using the Thomson scattering data alone (assuming $T_{\mathrm{i}} = T_{\mathrm{e}}$ and $n_{\mathrm{i}} = n_{\mathrm{e}}$) is 1.3 kJ. As was discussed above, edge $T_{\mathrm{i}}$ measurements in an inter-ELM period of a similar shot show that $T_{\mathrm{i}} \approx 2T_{\mathrm{e}}$. Assuming the profile change for the ions is the same as that measured for the electrons and using the measured average $Z$ effective over the pedestal region, $Z_{\mathrm{effective}} \approx 2$ (i.e. $n_{\mathrm{i}} = 0.8n_{\mathrm{e}}$, assuming fully stripped carbon) gives a measurement for the convective loss of 1.7 kJ. These measurements are consistent within errors with the changes in stored energy from EFIT $\Delta W = 1.4$ kJ.

Figure 23 shows the Thomson scattering profiles just before the ELM ($t_{\mathrm{ELM}} - 770\,\mu$s) and close to the ELM peak. The formation of a broad outboard tail in both the density and the

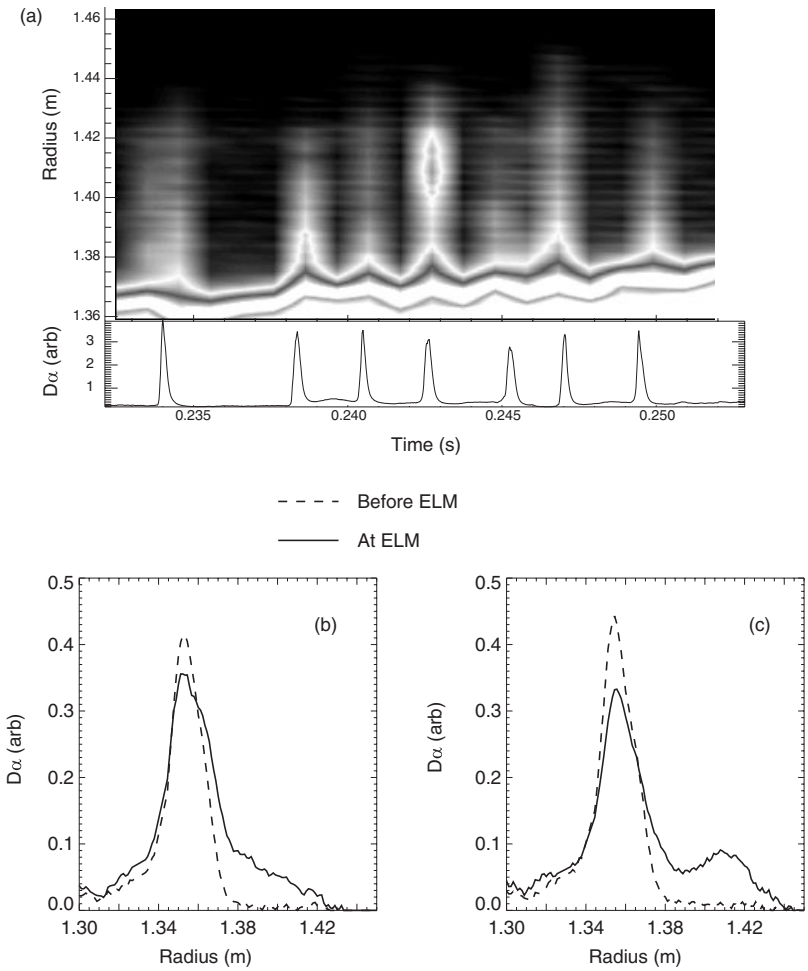


**Figure 24.** (*a*) The Abel inverted signal from a linear D$\alpha$ array viewing the outboard mid-plane plotted as radius versus time. The Abel inverted D$\alpha$ as a function of radius at the ELM peak (- - - -) and the neighbouring inter-ELM period (——) for (*b*) 0.233 s and (*c*) 0.242 s.

temperature can be observed at the outboard mid-plane (figures 23(*b*) and (*c*)), but no change is observed on the inboard side (figure 23(*a*)).

The broad tail witnessed on the Thomson scattering density profile at the outboard mid-plane during the ELM rise and observed to extend well beyond the inter-ELM separatrix is also seen on other diagnostics and is worthy of further mention. Figure 24(*a*) shows an Abel inversion of a linear D$\alpha$ camera signal viewing the outboard mid-plane. The D$\alpha$ emission, which is roughly Gaussian during inter-ELM periods, becomes strongly skewed to the outboard during the ELM with a tail typically extending at least 10 cm beyond the inter-ELM separatrix (figure 24(*b*)). On some ELMs a distinct feature is observed (figure 24(*a*) at $t = 0.242$ s and figure 24(*c*)). These features have also been observed in the Thomson scattering profiles. Figure 25 shows the Thomson scattering profile at the ELM peak for another discharge. At the outboard mid-plane, the density at the separatrix falls close to zero and then rises again 10 cm from the separatrix. While it is tempting to associate this feature with a 'blob' of plasma, there is no evidence from the targets that this 'blob' actually becomes detached.

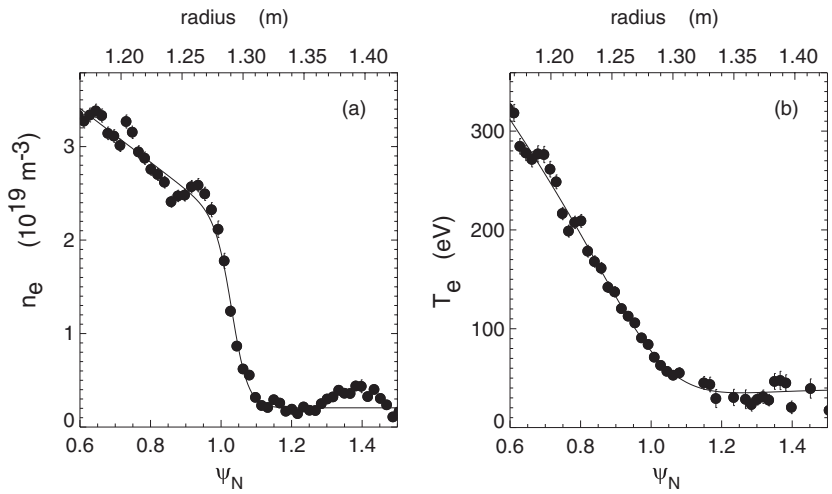


**Figure 25.** Thomson scattering profiles of the outboard edge density and temperature for a H-mode discharge, with neutral beam heating, at ($t_{\mathrm{ELM}} - 50\,\mu$s) with respect to the peak in the divertor D$\alpha$ emission for the ELM.

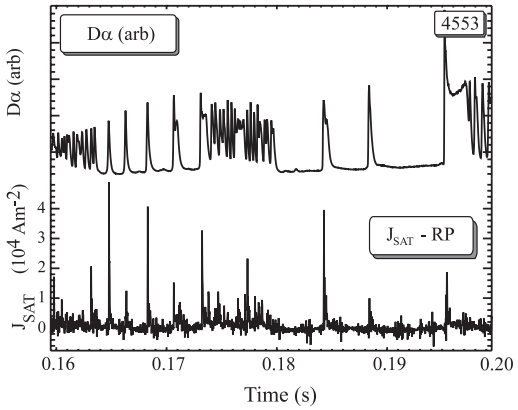


**Figure 26.** The D$\alpha$ signal and the $J_{\mathrm{SAT}}$ observed at the reciprocating probe 10 cm from the plasma edge for shot 4553.

ELM events are regularly observed with a reciprocating Langmuir probe at the outboard mid-plane, even up to 20 cm distant from the separatrix, $\Delta_r = 20$ cm. Figure 26 shows the ion saturation current density to the probe, $J_{\mathrm{SAT}}$, for a series of ELMs where the probe is 10 cm from the plasma edge. The $J_{\mathrm{SAT}}$ observed at the probe varies from ELM to ELM, and at times the probe does not see the ELM at all. The period of interaction with the reciprocating probe is typically around 50 $\mu$s (i.e. $\ll$ ELM peak in D$\alpha$ emission), with a rapid rise time of the order of 10 $\mu$s, and several distinct interactions are sometimes observed for what appears, from target D$\alpha$ emission, to be a single ELM. The maximum peak $J_{\mathrm{SAT}}$ observed is at least as large as values observed with probes embedded in the outboard divertor targets. Figure 27 shows a plot of the $J_{\mathrm{SAT}}$ current observed at the reciprocating probe and the divertor D$\alpha$ signal for three 'identical' shots where the probe was at 20, 10 and 3 cm from the plasma edge. The rise in $J_{\mathrm{SAT}}$ is delayed with respect to the rise in target D$\alpha$ emission. This delay increases with $\Delta_r$ and can be used to calculate a radial expansion velocity away from the separatrix, $v_r$.

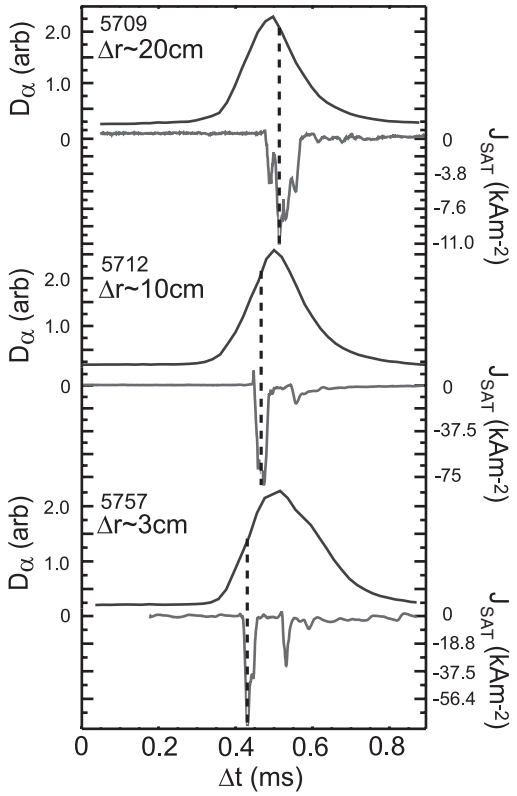


**Figure 27.** The D$\alpha$ signal and the $J_{\mathrm{SAT}}$ observed at the reciprocating probes for a set of identical discharges where the probe was at a different radial location with respect to the edge of the plasma.

Figure 28(*a*) shows a plot of the $J_{\mathrm{SAT}}$ as a function of distance between the probe and the plasma edge. Considerable $J_{\mathrm{SAT}}$ values can be observed for $\Delta_r \lesssim 10$–15 cm and can be still $>10\%$ of the target value up to 20 cm from the edge. Despite the long-range nature of this phenomenon at the mid-plane, no significant broadening of the particle or heat flux profiles at the divertor targets is observed during ELMs on MAST. This apparent contradiction will be returned to at the end of the section.

Figure 28(*b*) shows the frequency distribution of the calculated radial velocity, $v_r$ for ELMs from a variety of discharges. The mean $v_r$ is 750 m s$^{-1}$, but velocities up to 2 km s$^{-1}$ have been observed. The statistical variation in $v_r$ could be due to an unmeasured toroidal velocity component, and the spread in $J_{\mathrm{SAT}}$ at a given radius could be due to the dependence on the toroidal location of the probe with respect to where the ELM originates.

Apart from toroidally localized diagnostics such as the reciprocating probe, the vessel wall in MAST is remote from the plasma boundary (typically $>0.5$ m) and there is no obvious interaction during ELMs. Radial effluxes of similar extent and with a similar velocity have now been reported for ELMs on JET [31], which has a close fitting wall (typically a minimum of 30 cm from the plasma boundary to the outboard limiters), and could result in substantial interaction with, and erosion of, plasma facing components far from the divertor region.

A clear understanding of this phenomenon awaits future experiments and further analysis. The available evidence from MAST, however, is consistent with the hypothesis that the ELMs are associated with a high poloidal and toroidal mode number perturbation to the edge magnetic

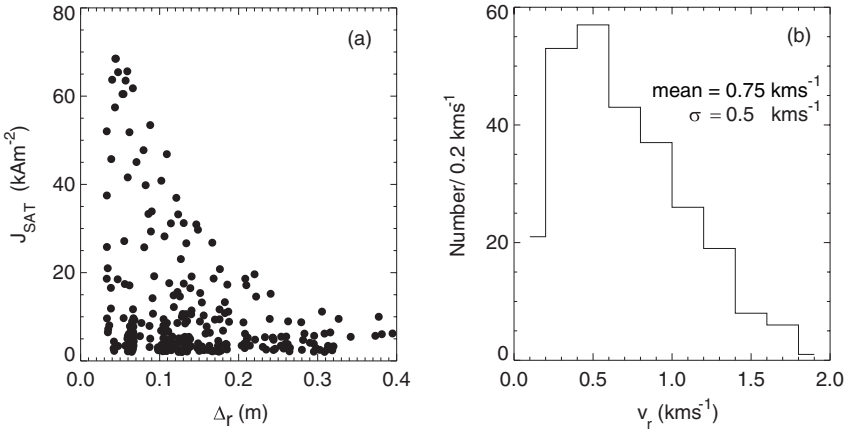


**Figure 28.** (*a*) Ion saturation current density of ELM efflux observed at the mid-plane reciprocating probe as a function of distance from the plasma edge. (*b*) The frequency distribution of the calculated radial expansion velocity calculated using the observed delay of the $J_{SAT}$ signal at the probe and the distance from the separatrix.

flux surfaces (consistent with observations on COMPASS-D using arrays of magnetic pick-up coils [32]), expanding away from the inter-ELM separatrix radius by at least 10 cm at up to 2 km s$^{-1}$. Such a perturbation would be localized to the edge of the core plasma, where it would appear to the mid-plane Thomson scattering and linear D$\alpha$ camera diagnostics as a broad outboard tail but would not in fact give rise to any significant broadening of the SOL flux tubes or the divertor target profiles [33]. That is, the ELM does not give rise to a broadening of the SOL or the bulk transport of material into the far SOL but rather it causes a rapid outboard movement of the SOL flux tubes coupled with enhanced transport across the separatrix in the convective channel, driven by a localized steepening of edge gradients. This is consistent with the predictions of a non-linear ballooning mode theory [34, 35].

## 5. Summary and conclusions

The ELM properties of a large ST have been characterized using the extensive edge diagnostics available on the MAST device. MAST typically operates close to an up–down symmetric double-null configuration, which is found to aid H-mode access. Type III ELM behaviour is observed even in the highest performance plasmas. High confinement is achieved in MAST at low ELM frequencies even though the ELMs exhibit many type III characteristics. These ELMs convect energy from the pedestal region predominantly to the low field side, collapsing the density pedestal and giving rise to a rapid radial outboard efflux, which can extend for some distance beyond the separatrix. The available evidence from MAST is consistent with the hypothesis that the ELM does not give rise to a broadening of the SOL or the transport of material into the far SOL but rather causes a rapid outboard movement of the SOL flux tubes around the core of the plasma, coupled with enhanced transport into the SOL in the convective channel.

The target balance observed in MAST is potentially rather favourable for the ST since H-mode access is facilitated in a region where ELM losses flow mostly to the large wetted area, outboard targets, and in addition, the target heat loads are reduced by an even distribution of power between the upper and lower targets.

## Acknowledgments

This work was funded jointly by the United Kingdom Engineering and Physical Sciences Research Council and by EURATOM. Dr Y Yang would also like to acknowledge a grant from the Royal Society.

## References

[1] Walsh M J *et al* 2003 *Rev. Sci. Instrum.* **74** 1663
[2] Walsh M J *et al* 2003 *Rev. Sci. Instrum.* **74** 1663–6
[3] Yang Y *et al* 2003 *J. Nucl. Mater.* **313–316** 734
[4] Kirk A *et al* 2003 *J. Nucl. Mater.* **313–316** 1081
[5] Counsell G *et al* 2002 *Plasma Phys. Control. Fusion* **44** 827
[6] Zohm H 1996 *Plasma Phys. Control. Fusion* **38** 105
[7] Connor J W 1998 *Plasma Phys. Control. Fusion* **40** 531
[8] Petrie T W *et al* 2001 *J. Nucl. Mater.* **290–293** 935
[9] Lao L L *et al* 1985 *Nucl. Fusion* **25** 1611
[10] Valovic M *et al* 1996 *Proc. 23rd EPS Conf. on Controlled Fusion and Plasma Physics* vol 20C, p 39
[11] ITER Physics Basis 1999 *Nucl. Fusion* **39** 2137
[12] Fishpool G M 1998 *Nucl. Fusion* **38** 1373
[13] Suttrop W *et al* 1997 *Plasma Phys. Control. Fusion* **39** 2051
[14] Kirk A *et al* 2004 H-mode pedestal characteristics on MAST *Plasma Phys. Control. Fusion* **46** at press
[15] Groebner R J and Carlstrom T N 1998 *Plasma Phys. Control. Fusion* **40** 673
[16] Mikhailovskii A B *et al* 1997 *Plasma Phys. Rep.* **23** 844
[17] Connor J W, Hastie R J, Wilson H R and Miller R L 1998 *Phys. Plasmas* **5** 2687
[18] Wilson H R, Snyder P B, Huysmans G T A and Miller R L 2002 *Phys. Plasmas* **9** 1277
[19] Connor J W, Hastie R J and Taylor J B 1979 *Proc. R. Soc. Lond.* A **365** 1
[20] Buttery R 2002 Stability at high performance in the MAST spherical tokamak *Proc. 19th IAEA Fusion Energy Conf. (Lyon, France, 14–19 October 2002)* (CD-ROM) paper EX/S1-6 and http://www.iaea.org/programmes/ripc/physics/fec2002/html/fec2002.htm
[21] Stangeby P C 2000 *Physics of Plasma–Wall Interactions in Controlled Fusion* (Bristol, UK: Institute of Physics)
[22] Doyle E J *et al* 1991 *Phys. Fluids* B **3** 2300
[23] Matthews G *et al* 2001 *J. Nucl. Mater.* **290–293** 668
[24] Herrmann A *et al* 1995 *Plasma Phys. Control. Fusion* **37** 17
[25] Eich T *et al* 2001 *Proc. 28th EPS Conf. on Plasma Phys. and Control. Fusion* vol 25A (ECA) p 1809
[26] Valovic M 2004 Energy Confinement in ELMy H-mode on MAST in preparation
[27] Matthews G F *et al* 2003 *J. Nucl. Mater.* **313–316** 986
[28] Loarte A *et al* 2000 Predicted ELM energy loss and power loading in ITER-FEAT *Proc. 18th IAEA Fusion Energy Conf. (Sorrento, Italy, 2000)* (CD-ROM) and http://www.iaea.org/programmes/ripc/physics/fec2000/html/node1.htm
[29] Matthews G *et al* 2002 Steady state and transient power handling in JET *Proc. 19th IAEA Fusion Energy Conf. (Lyon, France, 14–19 October 2002)* (CD-ROM) paper EX/D1-1 and http://www.iaea.org/programmes/ripc/physics/fec2002/html/fec2002.htm
[30] Jachmich S *et al* 2001 *Proc. 28th EPS Conf. on Plasma Phys. and Control. Fusion* vol 25A (ECA) p 1617
[31] Gonçalves B *et al* 2002 *Proc. 29th EPS Conf. on Plasma Phys. and Control. Fusion* vol 26B (ECA) O2.05
[32] Valovic M *et al* 1994 *Proc. 21st EPS Conf. on Plasma Phys. and Control. Fusion* p 318
[33] Cowley S C and Wilson H R 2003 I-1.2 Explosive instabilities: from solar flares to edge localized modes in tokamaks *Proc. 30th EPS Conf. on Control. Fusion and Plasma Phys. (St Petersburg, Russia)*
[34] Cowley S *et al* 1996 *Phys. Plasmas* **3** 1848
[35] Hurricane O A *et al* 1997 *Phys. Plasmas* **4** 3565